

Weak Localization and Antilocalization in Nodal-Line Semimetals: Dimensionality and Topological Effects

Wei Chen,^{1,2,*} Hai-Zhou Lu,^{3,4} and Oded Zilberberg¹

¹*Institute for Theoretical Physics, ETH Zurich, 8093 Zürich, Switzerland*

²*College of Science, Nanjing University of Aeronautics and Astronautics, Nanjing 210016, China*

³*Shenzhen Institute for Quantum Science and Engineering and Department of Physics, Southern University of Science and Technology, Shenzhen 518055, China*

⁴*Shenzhen Key Laboratory of Quantum Science and Engineering, Shenzhen 518055, China*

(Dated: August 15, 2022)

New materials such as nodal-line semimetals offer a unique setting for novel transport phenomena. Here, we calculate the quantum correction to conductivity in a disordered nodal-line semimetal. The torus-shaped Fermi surface and encircled π Berry flux carried by the nodal loop result in a fascinating interplay between the effective dimensionality of electron diffusion and band topology, which depends on the scattering range of the impurity potential relative to the size of the nodal loop. For a short-range impurity potential, backscattering is dominated by the interference paths that do not encircle the nodal loop, yielding a 3D weak localization effect. In contrast, for a long-range impurity potential, the electrons effectively diffuse in various 2D planes and the backscattering is dominated by the interference paths that encircle the nodal loop. The latter, leads to weak antilocalization with a 2D scaling law. Our results are consistent with symmetry consideration, where the two regimes correspond to the orthogonal and symplectic classes, respectively. Furthermore, we present weak-field magnetoconductivity calculations at low temperatures for realistic experimental parameters, and predict that clear scaling signatures $\propto \sqrt{B}$ and $\propto -\ln B$, respectively. The crossover between the 3D weak localization and 2D weak antilocalization can be probed by tuning the Fermi energy, giving a unique transport signature of the nodal-line semimetal.

The transport properties of materials can be well-approximated by taking into account conduction electrons moving in the presence of a periodic crystalline structure and using Bloch's theory. In the presence of strong disorder, however, this description breaks down and the electrons can localize, leading to Anderson insulators [1]. In fact, even weak disorder is sufficient to drive the electronic motion into the so-called quantum diffusive regime, resulting in weak localization (WL) [2], which is a precursor of the Anderson localization. WL is a quantum-mechanical effect where constructive interference between disorder-induced scattering events leads to increased backscattering. The inevitable presence of impurities in materials makes WL effects prominent in experiments, and has become the standard method used for measuring the phase coherence length, as well as its temperature dependence [3].

The WL quantum correction depends strongly on the specifics of the electronic system: (i) depending on the dimensionality of the system, the WL correction scales differently with the system size [2]; (ii) considering the symmetry class of the system in terms of time-reversal and spin-rotational symmetries, disorder can result in both WL and weak antilocalization (WAL) [4, 5]; and (iii) the geometrical and topological properties of the electronic bandstructure [6–8], can also lead to WAL [9–15]. A paradigmatic example of the latter is graphene, where the π Berry phase of the Dirac fermion changes the WL constructive interference into a WAL destructive one [16]. Interestingly, in the study of WL, the Fermi surface of the physical system is commonly taken to be a hypersphere

and the effects of dimensionality and band topology are unrelated.

Relatively new members to the topological phases of matter paradigm are nodal-line semimetals [17–35]. These 3D materials are characterized by bands that cross along closed loops that carry a π Berry flux [17]. A variety of candidates for nodal-line semimetals have been reported [18–24, 26–31], and their experimental characterization has seen recent progress using ARPES [31, 36–39] and quantum oscillation [40–44] measurements, alongside proposals for mesoscopic transport detection schemes [45]. In most nodal-line semimetals, the Fermi energy is lifted from the nodal line thus forming a torus-shaped Fermi surface that encircles the nodal line and its associated π Berry flux [46], see Fig. 1(a).

In this Letter, we analyze WL in nodal-line semimetals and find an interesting interplay between the dimensionality of diffusion and the band topology. We consider two types of disorder with either short-range (SR) or long-range (LR) impurity potentials relative to the size of the nodal loop. In the SR limit, the so-called white-noise disorder-induced scattering equally couples all states on the Fermi surface, and WL backscattering is dominated by interference along the toroidal direction, see Fig. 1(c). Such an interference loop does not encircle the nodal line and its associated π Berry flux. Correspondingly, the electrons diffuse in the full 3D phase-space resulting in 3D WL, similarly to anisotropic conventional metals. The LR limit, can occur due to unconventional screening effects [47]. Here, backscattering is dominated by interference along the poloidal direction in reciprocal space

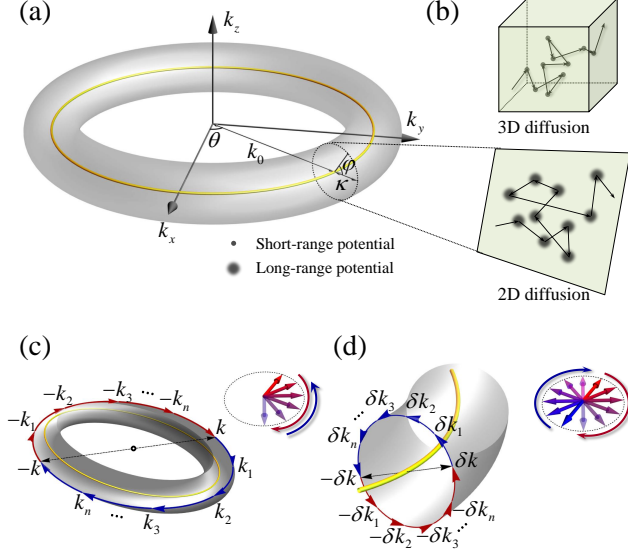


FIG. 1. Backscattering processes in nodal-line semimetals. (a) Torus-shaped Fermi surface of nodal-line semimetals, with major radius k_0 , minor radius κ , toroidal angle θ , and poloidal angle φ . (b) The real-space range of the impurity potentials results in 3D and 2D diffusion behaviors, for short-range and long-range impurities, respectively. (c) A coherent backscattering from wavevector \mathbf{k} to $-\mathbf{k}$ around the toroidal direction is possible for short-ranged impurity potentials via intermediate states $(\mathbf{k}_1, \mathbf{k}_2, \dots, \mathbf{k}_n)$ and its time-reversed counterpart $(-\mathbf{k}_n, -\mathbf{k}_{n-1}, \dots, -\mathbf{k}_1)$. In the circular inset, blue and red arrows depict that the net spinor rotation around the interference path is zero. (d) Backscattering from wavevector $\delta\mathbf{k}$ to $-\delta\mathbf{k}$ along the poloidal direction is the dominant process under long-ranged impurity potentials. Here, the net spinor rotation is 2π , contributing a π Berry phase to backscattering, and results in weak antilocalization.

that encircles the nodal line, see Fig. 1(d). As a result, we predict that a WAL correction will occur. Importantly, despite the 3D nature of the system, the WAL correction shows a 2D scaling behavior. In the LR scenario, the WAL conductivity correction is proportional to the circumference of the nodal line, or equivalently, to the number of 2D diffusion planes. We discuss possible detection of our prediction using magnetoconductivity experiments, in which tuning the Fermi energy can induce a crossover between the 3D WL and 2D WAL.

Nodal-line semimetals can be generally described by an effective two-band model

$$H = \hbar\lambda(k_x^2 + k_y^2 - k_0^2)\tau_x + \hbar v k_z \tau_y, \quad (1)$$

where $\tau_{x,y}$ are the Pauli matrices corresponding to two bands that cross at $k_x^2 + k_y^2 = k_0^2, k_z = 0$, and define a nodal loop. For a Fermi energy that satisfies $E_F \ll \hbar\lambda k_0^2$, the Hamiltonian (1) can be linearized and parametrized to the simple form

$$\mathcal{H} = \hbar v_0 \kappa (\cos \varphi \tau_x + \sin \varphi \tau_y) \quad (2)$$

through the substitution $k_x = (k_0 + \kappa \cos \varphi) \cos \theta, k_y = (k_0 + \kappa \cos \varphi) \sin \theta, k_z = \kappa \sin \varphi / \alpha$, with $v_0 = 2\lambda k_0$, and $\alpha = v/v_0$ the ratio between the velocity along the z -direction and the velocity in the $x-y$ plane. The parameters κ, θ, φ are labeled in Fig. 1(a). For the purposes of this work, we assume that E_F intersects with the conduction band, and solely include it in the analysis below. The dispersion of the conduction band is $\varepsilon_{\mathbf{k}} = \hbar v_0 \kappa$ and its corresponding wavefunction is $\psi_{\mathbf{k}}(\mathbf{r}) = [1, e^{i\varphi}]^T e^{i\mathbf{k} \cdot \mathbf{r}} / \sqrt{2V}$, with V the volume of the system. The density of states at the Fermi energy is $\rho_0 = \mathcal{K} E_F / (\alpha \hbar^2 v_0^2)$, which is proportional to the circumference $\mathcal{K} = 2\pi k_0$ of the nodal loop.

The nodal-line semimetal possesses two types of antiunitary symmetries $\mathcal{T}_1 = K$ and $\mathcal{T}_2 = i\tau_y K$ with K the complex conjugation, such that

$$\mathcal{T}_1 \mathcal{H}(\mathbf{k}) \mathcal{T}_1^{-1} = \mathcal{H}(-\mathbf{k}), \quad (3a)$$

$$\mathcal{T}_2 \mathcal{H}(\delta\mathbf{k}) \mathcal{T}_2^{-1} = \mathcal{H}(-\delta\mathbf{k}), \quad (3b)$$

where the small momentum $\delta\mathbf{k} = \kappa(\cos \varphi, \sin \varphi / \alpha)$ is defined in a local poloidal plane in momentum space denoted by the toroidal angle θ , see Fig. 1(a). Note that \mathcal{T}_1 is the spinless time-reversal symmetry while \mathcal{T}_2 is a local antiunitary symmetry containing a spin inversion. The latter can be regarded as the spinful time-reversal symmetry for the 2D subsystem defined by θ , see Fig. 1(b). According to symmetry classification, \mathcal{T}_1 and \mathcal{T}_2 belong to the orthogonal and symplectic classes, respectively [4, 5]. Hence, they respectively lead to WL and WAL depending on which physical process dominates the backscattering [cf. Figs. 1(c) and 1(d)].

The dominant process that leads to backscattering is determined by the type of disorder, and by the size of the nodal loop. The disorder potential is expressed by $U(\mathbf{r}) = \sum_j u(\mathbf{r} - \mathbf{R}_j)$, where \mathbf{R}_j are the positions of the randomly distributed impurities. Without loss of generality, we set the uniform background of the impurity potential to zero, $\langle U(\mathbf{r}) \rangle_{\text{imp}} = 0$, where $\langle \dots \rangle_{\text{imp}}$ denotes averaging over impurity configurations. Commonly, the white-noise disorder (SR limit) is considered, i.e., an impurity-potential with constant scattering-strength in reciprocal space [2]. Here, we investigate a more general case where $\langle U(\mathbf{k}) U(-\mathbf{k}') \rangle_{\text{imp}} = (2\pi)^3 n_i |u_{\mathbf{k}}|^2 \delta(\mathbf{k} - \mathbf{k}')$ with $U(\mathbf{k})$ [$u_{\mathbf{k}}$] the Fourier component of $U(\mathbf{r})$ [$\mathcal{U}(\mathbf{r})$], and n_i the concentration of the impurities. Associating a finite scattering-range to the impurities, r_{sc} , results in a confinement of the allowed scattering processes in reciprocal space. We consider E_F sufficiently low such that $k_0 \gg 1/r_{\text{sc}} \gg \kappa$, and therefore the scattering strength between different \mathbf{k} states can be well characterized solely by θ . For simplicity, we further assume that $u_{\mathbf{k}} = u(\theta) = u_0 f_{\Delta}(\theta)$ with $f_{\Delta}(x) = \Theta(x + \Delta) \Theta(-x + \Delta)$, and $\Theta(x)$ the Heaviside step function. This choice of potential yields the SR limit when $\Delta = \pi$, whereas the LR limit corresponds to $\Delta \rightarrow 0$.

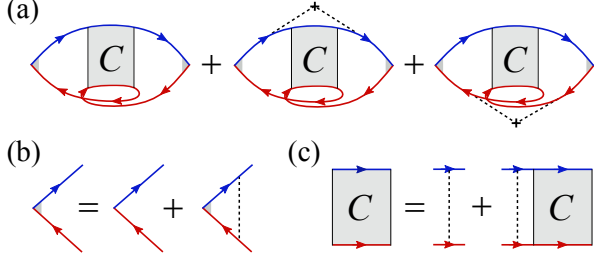


FIG. 2. Relevant Feynman diagrams. (a) Leading diagrams contributing to the quantum interference correction to conductivity, containing one bare and two dressed Hikami boxes, cf. Eq. (4) and Ref. [3]. The arrowed solid and dashed lines represent Green's functions and impurity scattering, respectively. The gray box marks the Cooperon ladder propagator. (b) Ladder diagram vertex correction to the velocity. (c) Diagrammatic representation of the Bethe-Salpeter equation for the Cooperon correction.

We calculate the quantum interference correction to the conductivity along the z -axis using Feynman diagrams [48], see Fig. 2(a). In our calculation, we include the three leading-order diagrams, namely, the bare Hikami box [5], and two dressed Hikami boxes [10, 49]. The latter two jointly contribute $-1/2$ the correction of the former for both the SR and LR limits [50], similar to the case in graphene [10]. Thus, the overall quantum correction to the zero-temperature conductivity is [3]

$$\sigma_z = s\eta_z^2 \frac{e^2 \hbar}{4\pi V^2} \sum_{\mathbf{k}, \mathbf{k}'} v_{\mathbf{k}}^z v_{\mathbf{k}'}^z G_{\mathbf{k}}^R G_{\mathbf{k}}^A G_{\mathbf{k}'}^R G_{\mathbf{k}'}^A C_{\mathbf{k}, \mathbf{k}'}, \quad (4)$$

where $s = 2$ accounts for the spin degeneracy, $\eta_z = 2$ is the factor coming from the vertex correction to the velocity $v_{\mathbf{k}}^z$ [cf. Fig. 2(b) and Ref. [50]]. The impurity-averaged retarded (R) and advanced (A) Green's functions are solved under the first-order Born approximation, $G_{\mathbf{k}}^{R,A}(\omega) = 1/[\omega - \varepsilon_{\mathbf{k}} \pm i\hbar/(2\tau_e)]$, with the elastic scattering time $\tau_e = 2\hbar/(n_i \rho_0 \tilde{u}^2)$, and $\tilde{u}^2 = \int_0^{2\pi} d\theta |u(\theta)|^2$ [50]. Last, $C_{\mathbf{k}, \mathbf{k}'}$ is the full Cooperon satisfying the Bethe-Salpeter equation for the ladder of maximally-crossed diagrams [3], see Fig. 2(c).

As a function of the impurity potential different interference loops are available in reciprocal space, see Figs. 1(c) and 1(d). Correspondingly, the Bethe-Salpeter equation for the Cooperon will be dominated by different processes. In the SR limit $\Delta = \pi$, the majority of backscattering trajectories come in pairs via the intermediate states $(\mathbf{k}_1, \mathbf{k}_2, \dots, \mathbf{k}_n)$ and their time-reversed counterpart $(-\mathbf{k}_n, -\mathbf{k}_{n-1}, \dots, -\mathbf{k}_1)$, as imposed by \mathcal{T}_1 . Importantly, these trajectories do not encircle the nodal line. The corresponding Bethe-Salpeter equation is $C_{\mathbf{k}, \mathbf{k}'} = C_{\mathbf{k}, \mathbf{k}'}^0 + \frac{1}{V} \sum_{\mathbf{k}_1} C_{\mathbf{k}, \mathbf{k}_1} G_{\mathbf{k}_1}^R G_{\mathbf{Q}-\mathbf{k}_1}^A C_{\mathbf{k}_1, \mathbf{k}'}^0$, where the bare Cooperon is $C_{\mathbf{k}, \mathbf{k}'}^0 = \langle \tilde{U}_{\mathbf{k}, \mathbf{k}'} \tilde{U}_{-\mathbf{k}, -\mathbf{k}'} \rangle_{\text{imp}} / V = \gamma \cos^2 \frac{\varphi - \varphi'}{2}$, with $\gamma = n_i u_0^2$, the momentum $\mathbf{Q} = \mathbf{k} + \mathbf{k}'$,

and $\tilde{U}_{\mathbf{k}, \mathbf{k}'} = \langle \psi_{\mathbf{k}}(\mathbf{r}) | U(\mathbf{r}) | \psi_{\mathbf{k}'}(\mathbf{r}) \rangle$. Solving the Bethe-Salpeter equations self-consistently and keeping the most divergent contributions for $\mathbf{Q} \rightarrow 0$ yields in the DC-limit ($\omega \rightarrow 0$) [50]

$$C_{\mathbf{k}, \mathbf{k}'} = \frac{\gamma}{2\tau_e} \frac{1}{D_{xy} Q_{xy}^2 + D_z Q_z^2}, \quad (5)$$

where $Q_{xy} = \sqrt{Q_x^2 + Q_y^2}$, and $D_{xy} = v_0^2 \tau_e / 4$, $D_z = \alpha^2 v_0^2 \tau_e$ are diffusion coefficients in the $x - y$ plane and z -direction, respectively. We obtain that the Cooperon in the SR limit (5) shows a 3D WL behavior similar to an anisotropic normal metal [3].

In the LR limit $\Delta \rightarrow 0$, the aforementioned backscattering channel is suppressed and the quantum correction is dominated by interference trajectories $(\delta \mathbf{k}_1, \delta \mathbf{k}_2, \dots, \delta \mathbf{k}_n)$ and $(-\delta \mathbf{k}_n, -\delta \mathbf{k}_{n-1}, \dots, -\delta \mathbf{k}_1)$, which are paired by the \mathcal{T}_2 symmetry and form a small loop that encircles the nodal line. In this case, the iterative equation becomes $C_{\delta \mathbf{k}, \delta \mathbf{k}'} = C_{\delta \mathbf{k}, \delta \mathbf{k}'}^0 + \frac{1}{V} \sum_{\delta \mathbf{k}_1} C_{\delta \mathbf{k}, \delta \mathbf{k}_1} G_{\delta \mathbf{k}_1}^R G_{\mathbf{q}-\delta \mathbf{k}_1}^A C_{\delta \mathbf{k}_1, \delta \mathbf{k}'}^0$, with the bare Cooperon $C_{\delta \mathbf{k}, \delta \mathbf{k}'}^0 = \langle \tilde{U}_{\delta \mathbf{k}, \delta \mathbf{k}'} \tilde{U}_{-\delta \mathbf{k}, -\delta \mathbf{k}'} \rangle_{\text{imp}} / V = (\gamma/4) f_{\Delta}(\theta - \theta') [1 + 2e^{-i(\varphi - \varphi')} + e^{-2i(\varphi - \varphi')}]$ and momentum $\mathbf{q} = \delta \mathbf{k} + \delta \mathbf{k}'$ measured from the nodal line in the plane labeled by θ . Solving the Bethe-Salpeter equations in this case for $\mathbf{q} \rightarrow 0$ yields in the DC-limit [50]

$$C_{\delta \mathbf{k}, \delta \mathbf{k}'} = \frac{\gamma}{2\tau_e} \frac{f_{\Delta}(\theta - \theta') e^{-i(\varphi - \varphi')}}{4D_{xy} q_{xy}^2 \cos^2(\theta_q - \theta) + D_z q_z^2}, \quad (6)$$

where $q_{xy} = \sqrt{q_x^2 + q_y^2}$. The scattering here always occurs accompanied with a spin rotation [see Fig. 1(d)], which is the source of the additional geometric phase $e^{-i(\varphi - \varphi')}$. This geometrical phase leads to the suppression of backscattering ($\varphi - \varphi' = \pi$) and to WAL [9]. The result (6) contains two θ -dependent factors. Hence, for $\Delta \rightarrow 0$ and through $f_{\Delta}(\theta - \theta')$, the scattering occurs between states that lie in the same poloidal plane. Conjointly, the divergent term $\cos^2(\theta_q - \theta)$ vanishes when $\theta_q - \theta = \pi/2$, thus implying that diffusion cannot happen in the direction perpendicular to the θ plane. Combining the above observations, we can reach the intriguing conclusion that in the LR limit electrons exhibit a 2D quantum diffusion [cf. Fig. 1(b)].

Inserting the Cooperon expressions into Eq. (4), we obtain the correction to the conductivity in both the SR and LR limits [50]

$$\sigma_z^S = -\frac{s\eta_z^2 \alpha e^2}{2\pi^2 \hbar} \left(\frac{1}{\ell_e} - \frac{1}{\ell_{\phi}} \right), \quad (7a)$$

$$\sigma_z^L = \frac{s\eta_z^2 \mathcal{K} \alpha e^2}{2(2\pi)^2 \hbar} \ln(\ell_{\phi}/\ell_e), \quad (7b)$$

respectively. Here, $\ell_e = v_0 \tau_e$ is the mean free path, and ℓ_{ϕ} is the phase coherence length. In the SR limit, a

3D scaling is obtained for the quantum correction and the overall minus sign indicates WL. In contrast, the LR correction is positive (WAL) and has a 2D scaling law. The prefactor \mathcal{K} in σ_z^L ensures the unit of 3D conductivity and also enhances the WAL correction contributed by a large number of 2D diffusion planes. Due to the different dimensionality of the scaling, σ_z^S will saturate as $\ell_\phi \rightarrow \infty$; in contrast, σ_z^L always increases as $\ln(\ell_\phi/\ell_e)$ due to the 2D diffusion.

The disorder-induced quantum correction to conductivity is suppressed by magnetic field induced dephasing [3]. This allows one to experimentally observe the WL and WAL corrections using magnetoconductivity measurements. To calculate the impact of the magnetic field, we impose a quantization condition to the component of \mathbf{Q}, \mathbf{q} perpendicular to the magnetic field, i.e., $Q_\perp, q_\perp = (n + 1/2)(4eB/\hbar) \equiv (n + 1/2)/\ell_B^2$, where ℓ_B is the magnetic length. In the SR regime, since the diffusion is 3D, the magnetic field along any direction will lead to dephasing; here we set it to the z -direction. For the LR regime, electrons move in different planes parallel to the z -axis. Thus, a magnetic field along the z -direction cannot lead to dephasing and we align it along the x -direction. We substitute the quantized values of Q_\perp, q_\perp into the Cooperon [Eq. (4)] and obtain the resulting magnetoconductivity $\delta\sigma_z^{S,L}(B) \equiv \sigma_z^{S,L}(B) - \sigma_z^{S,L}(0)$, with

$$\sigma_z^S(B) = -\frac{s\eta_z^2\alpha e^2}{(2\pi)^2\hbar} \left[\Psi(\ell_B^2/\ell_e^2 + \frac{1}{2})/\ell_e - \Psi(\ell_B^2/\ell_\phi^2 + \frac{1}{2})/\ell_\phi - \int_{1/\ell_\phi}^{1/\ell_e} dx \Psi(\ell_B^2 x^2 + \frac{1}{2}) \right], \quad (8a)$$

$$\sigma_z^L(B) = \frac{s\eta_z^2\mathcal{K}\alpha e^2}{16\pi^2\hbar} \int_0^{2\pi} \frac{d\theta}{2\pi} \left[\Psi\left(\frac{\ell_B^2}{\ell_e^2\alpha|\sin\theta|} + \frac{1}{2}\right) - \Psi\left(\frac{\ell_B^2}{\ell_\phi^2\alpha|\sin\theta|} + \frac{1}{2}\right) \right], \quad (8b)$$

where $\Psi(x)$ is the digamma function [50]. In the zero-field limit $B \rightarrow 0$, the results in Eqs. (8) reduce to that of Eqs. (7). The average integral over θ in Eq. (8b) arises from the fact that electrons in different diffusion planes feel different magnetic fields perpendicular to the respective plane.

In Fig. 3, we plot our magnetoconductivity predictions [Eqs. (8)], where the integrals are evaluated numerically. The WL effect in the SR regime leads to a positive magnetoconductivity [Fig. 3(a)], while the WAL effect in the LR regime is revealed by negative magnetoconductivity [Fig. 3(b)]. We plot the results for various values of ℓ_ϕ , which can be tuned by the temperature of the experiment. At low temperatures, $\ell_\phi \gg \ell_B$ since $\ell_\phi \sim 100\text{nm} - 1\mu\text{m}$ and $\ell_B \sim 10\text{nm}$ when $B \sim 0.1 - 1\text{T}$. The magnetoconductivity in the two scenarios exhibit a different B -dependence at low temperatures. Specifically, $\delta\sigma_z^S(B) \propto \sqrt{B}$ in the SR regime and $\delta\sigma_z^L(B) \propto -\ln B$ in the LR regime, see fitted dashed lines in Fig. 3. Im-

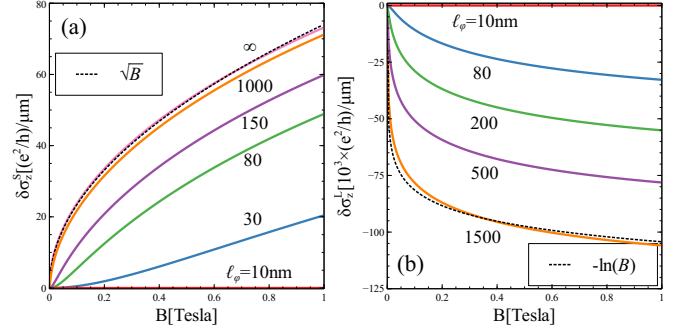


FIG. 3. The magnetoconductivity $\delta\sigma_z(B)$ in the (a) SR limit [cf. Eq. (8a)] and (b) LR limit [cf. Eq. (8b)] for different phase coherence lengths ℓ_ϕ . The mean free path is set to $\ell_e = 10\text{nm}$. The magnetic length is taken to be $\ell_B \simeq 12.8\text{nm}/\sqrt{B}$ with B in Tesla. In (b) $\mathcal{K} = 50\text{nm}^{-1}$ and $\alpha = 5$ are used.

portantly, the $\ln B$ dependence in the LR limit agrees with our 2D diffusion prediction [2], which occurs in a 3D system. Usually, 2D diffusion results in a much larger WL/WAL effect than in 3D diffusion. Moreover, the 3D nature of the nodal-line semimetal contains a large number of 2D effective subsystems, which also significantly enhance the magnetoconductivity [51]. Indeed, we observe in Fig. 3 that for reasonable physical parameters, $\delta\sigma_z^L(B)$ is three orders larger than $\delta\sigma_z^S(B)$, indicating a very strong signature of WAL in the LR regime.

Our analysis provides a concrete prediction for the impact of weak disorder on transport in nodal-line semimetals. Current experiments are focused on quantum oscillations in a strong magnetic field [41, 42, 52–57], and no WL study on nodal-line semimetals has been reported so far. Our predicted two limits leading to 3D WL and 2D WAL will manifest differently depending on the type of impurity potentials in the material, and relative to the size of the nodal loop. In real nodal-line semimetals, the impurity potential is predicted to be of LR-type due to unconventional screening effects [47]. Local scattering in the reciprocal space that leads to WAL is well-defined only when $\kappa \ll k_0$ [cf. Fig. 1(a)]. Otherwise, if κ and k_0 are of the same order, the two kinds of backscattering will coexist (due to toroidal and poloidal interference trajectories), and hence 3D WL will dominate the transport which stems from the larger 3D phase space for scattering along the toroidal direction. As a result, a large nodal loop and a low Fermi energy E_F above the nodal loop is favorable for 2D WAL. As E_F increases, κ increases, and WL will overcome WAL. Furthermore, by increasing E_F , the Fermi surface and the WAL interference loop [Fig. 1(d)] may undergo various warping, similar to the trigonal warping in graphene [10], thus breaking the \mathcal{T}_2 symmetry, and further suppressing the 2D WAL. Nevertheless, as long as the warping does not break time reversal symmetry \mathcal{T}_1 , the 3D WL will survive. Consequently, we predict a crossover from 2D WAL to 3D WL

to occur by tuning E_F , e.g., by doping or gate tuning on a thin-film sample. This is a unique effect arising from the torus-shaped Fermi surface and the Berry flux in nodal-line semimetals.

We thank J. L. Lado and Fengqi Song for helpful discussions. W. C. acknowledges the support from the National Natural Science Foundation of China under Grants No. 11504171, and the Swiss Government Excellence Scholarship under the program of China Scholarships Council (No. 201600160112). O. Z. thanks the Swiss National Science Foundation for financial support. H. L. is supported by the Guangdong Innovative and Entrepreneurial Research Team Program (2016ZT06D348), the National Key R & D Program (2016YFA0301700), the National Natural Science Foundation of China (11574127), and the Science, Technology and Innovation Commission of Shenzhen Municipality (ZDSYS20170303165926217, JCYJ20170412152620376).

* pchenweis@gmail.com

- [1] P. W. Anderson, Phys. Rev. **109**, 1492 (1958).
- [2] P. A. Lee and T. V. Ramakrishnan, Rev. Mod. Phys. **57**, 287 (1985).
- [3] E. Akkermans and G. Montambaux, *Mesoscopic physics of electrons and photons* (Cambridge university press, 2007).
- [4] F. J. Dyson, Journal of Mathematical Physics **3**, 140 (1962).
- [5] S. Hikami, A. I. Larkin, and Y. Nagaoka, Progress of Theoretical Physics **63**, 707 (1980).
- [6] M. Z. Hasan and C. L. Kane, Rev. Mod. Phys. **82**, 3045 (2010).
- [7] X.-L. Qi and S.-C. Zhang, Rev. Mod. Phys. **83**, 1057 (2011).
- [8] T. Ozawa, H. M. Price, A. Amo, N. Goldman, M. Hafezi, L. Lu, M. Rechtsman, D. Schuster, J. Simon, O. Zilberberg, *et al.*, arXiv preprint arXiv:1802.04173 (2018).
- [9] H. Suzuura and T. Ando, Phys. Rev. Lett. **89**, 266603 (2002).
- [10] E. McCann, K. Kechedzhi, V. I. Fal'ko, H. Suzuura, T. Ando, and B. L. Altshuler, Phys. Rev. Lett. **97**, 146805 (2006).
- [11] H.-Z. Lu, J. Shi, and S.-Q. Shen, Phys. Rev. Lett. **107**, 076801 (2011).
- [12] I. Garate and L. Glazman, Phys. Rev. B **86**, 035422 (2012).
- [13] H.-Z. Lu and S.-Q. Shen, Phys. Rev. Lett. **112**, 146601 (2014).
- [14] H.-Z. Lu and S.-Q. Shen, Phys. Rev. B **92**, 035203 (2015).
- [15] X. Dai, H.-Z. Lu, S.-Q. Shen, and H. Yao, Phys. Rev. B **93**, 161110 (2016).
- [16] T. Ando, T. Nakanishi, and R. Saito, Journal of the Physical Society of Japan **67**, 2857 (1998).
- [17] A. A. Burkov, M. D. Hook, and L. Balents, Phys. Rev. B **84**, 235126 (2011).
- [18] Y. Kim, B. J. Wieder, C. L. Kane, and A. M. Rappe, Phys. Rev. Lett. **115**, 036806 (2015).
- [19] R. Yu, H. Weng, Z. Fang, X. Dai, and X. Hu, Phys. Rev. Lett. **115**, 036807 (2015).
- [20] T. T. Heikkilä, N. B. Kopnin, and G. E. Volovik, JETP Letters **94**, 233 (2011).
- [21] H. Weng, Y. Liang, Q. Xu, R. Yu, Z. Fang, X. Dai, and Y. Kawazoe, Phys. Rev. B **92**, 045108 (2015).
- [22] Y. Chen, Y. Xie, S. A. Yang, H. Pan, F. Zhang, M. L. Cohen, and S. Zhang, Nano Letters **15**, 6974 (2015).
- [23] M. Zeng, C. Fang, G. Chang, Y.-A. Chen, T. Hsieh, A. Bansil, H. Lin, and L. Fu, arXiv:1504.03492 [cond-mat] (2015), arXiv: 1504.03492.
- [24] C. Fang, Y. Chen, H.-Y. Kee, and L. Fu, Phys. Rev. B **92**, 081201 (2015).
- [25] K. Mullen, B. Uchoa, and D. T. Glatzhofer, Phys. Rev. Lett. **115**, 026403 (2015).
- [26] A. Yamakage, Y. Yamakawa, Y. Tanaka, and Y. Okamoto, Journal of the Physical Society of Japan **85**, 013708 (2016).
- [27] L. S. Xie, L. M. Schoop, E. M. Seibel, Q. D. Gibson, W. Xie, and R. J. Cava, APL Materials **3**, 083602 (2015).
- [28] Y.-H. Chan, C.-K. Chiu, M. Y. Chou, and A. P. Schnyder, Phys. Rev. B **93**, 205132 (2016).
- [29] J. Zhao, R. Yu, H. Weng, and Z. Fang, Phys. Rev. B **94**, 195104 (2016).
- [30] G. Bian, T.-R. Chang, H. Zheng, S. Velury, S.-Y. Xu, T. Neupert, C.-K. Chiu, S.-M. Huang, D. S. Sanchez, I. Belopolski, N. Alidoust, P.-J. Chen, G. Chang, A. Bansil, H.-T. Jeng, H. Lin, and M. Z. Hasan, Phys. Rev. B **93**, 121113 (2016).
- [31] G. Bian, T.-R. Chang, R. Sankar, S.-Y. Xu, H. Zheng, T. Neupert, C.-K. Chiu, S.-M. Huang, G. Chang, I. Belopolski, D. S. Sanchez, M. Neupane, N. Alidoust, C. Liu, B. Wang, C.-C. Lee, H.-T. Jeng, C. Zhang, Z. Yuan, S. Jia, A. Bansil, F. Chou, H. Lin, and M. Z. Hasan, Nature Communications **7**, 10556 (2016).
- [32] T. Bzdušek, Q. Wu, A. Rüegg, M. Sigrist, and A. A. Soluyanov, Nature **538**, 75 (2016), letter.
- [33] W. Chen, H.-Z. Lu, and J.-M. Hou, Phys. Rev. B **96**, 041102 (2017).
- [34] Z. Yan, R. Bi, H. Shen, L. Lu, S.-C. Zhang, and Z. Wang, Phys. Rev. B **96**, 041103 (2017).
- [35] M. Ezawa, Phys. Rev. B **96**, 041202 (2017).
- [36] L. M. Schoop, M. N. Ali, C. Straßer, A. Topp, A. Varykhalov, D. Marchenko, V. Duppel, S. S. P. Parkin, B. V. Lotsch, and C. R. Ast, **7**, 11696 (2016).
- [37] M. Neupane, I. Belopolski, M. M. Hosen, D. S. Sanchez, R. Sankar, M. Szlowska, S.-Y. Xu, K. Dimitri, N. Dhakal, P. Maldonado, P. M. Oppeneer, D. Kaczorowski, F. Chou, M. Z. Hasan, and T. Durakiewicz, Phys. Rev. B **93**, 201104 (2016).
- [38] A. Topp, J. M. Lippmann, A. Varykhalov, V. Duppel, B. V. Lotsch, C. R. Ast, and L. M. Schoop, New Journal of Physics **18**, 125014 (2016).
- [39] D. Takane, Z. Wang, S. Souma, K. Nakayama, C. X. Trang, T. Sato, T. Takahashi, and Y. Ando, Phys. Rev. B **94**, 121108 (2016).
- [40] J. Hu, Z. Tang, J. Liu, X. Liu, Y. Zhu, D. Graf, K. Myhro, S. Tran, C. N. Lau, J. Wei, and Z. Mao, Phys. Rev. Lett. **117**, 016602 (2016).
- [41] J. Hu, Y. L. Zhu, D. Graf, Z. J. Tang, J. Y. Liu, and Z. Q. Mao, Phys. Rev. B **95**, 205134 (2017).
- [42] N. Kumar, K. Manna, Y. Qi, S.-C. Wu, L. Wang, B. Yan, C. Felser, and C. Shekhar, Phys. Rev. B **95**, 121109 (2017).
- [43] H. Pan, B. Tong, J. Yu, J. Wang, D. Fu, S. Zhang,

- B. Wu, X. Wan, C. Zhang, X. Wang, and F. Song, arXiv:1708.02779 [cond-mat] (2017), arXiv: 1708.02779.
- [44] C. Li, C. M. Wang, B. Wan, X. Wan, H.-Z. Lu, and X. C. Xie, Phys. Rev. Lett. **120**, 146602 (2018).
- [45] W. Chen, K. Luo, L. Li, and O. Zilberberg, Phys. Rev. Lett. **121**, 166802 (2018).
- [46] D. Takane, K. Nakayama, S. Souma, T. Wada, Y. Okamoto, K. Takenaka, Y. Yamakawa, A. Yamakage, T. Mitsuhashi, K. Horiba, *et al.*, npj Quantum Materials **3**, 1 (2018).
- [47] S. V. Syzranov and B. Skinner, Phys. Rev. B **96**, 161105 (2017).
- [48] The Fermi surface of the nodal-line semimetal is anisotropic and generates an anisotropic conductivity. Nevertheless, the qualitative difference between the calculated WL and WAL corrections do not change with the transport direction.
- [49] O. Chalaev and D. Loss, Phys. Rev. B **71**, 245318 (2005).
- [50] See Supplemental Material for additional details.
- [51] H. Cao, J. Tian, I. Miotkowski, T. Shen, J. Hu, S. Qiao, and Y. P. Chen, Phys. Rev. Lett. **108**, 216803 (2012).
- [52] H. Pan, B. Tong, J. Yu, J. Wang, D. Fu, S. Zhang, B. Wu, X. Wan, C. Zhang, X. Wang, *et al.*, Scientific Reports (Nature Publisher Group) **8**, 1 (2018).
- [53] X. Wang, X. Pan, M. Gao, J. Yu, J. Jiang, J. Zhang, H. Zuo, M. Zhang, Z. Wei, W. Niu, *et al.*, Advanced Electronic Materials **2**, 1600228 (2016).
- [54] Y.-Y. Lv, B.-B. Zhang, X. Li, S.-H. Yao, Y. Chen, J. Zhou, S.-T. Zhang, M.-H. Lu, and Y.-F. Chen, Applied Physics Letters **108**, 244101 (2016).
- [55] M. N. Ali, L. M. Schoop, C. Garg, J. M. Lippmann, E. Lara, B. Lotsch, and S. S. Parkin, Science advances **2**, e1601742 (2016).
- [56] J. Zhang, M. Gao, J. Zhang, X. Wang, X. Zhang, M. Zhang, W. Niu, R. Zhang, and Y. Xu, Frontiers of Physics **13**, 137201 (2018).
- [57] S. Li, Z. Guo, D. Fu, X.-C. Pan, J. Wang, K. Ran, S. Bao, Z. Ma, Z. Cai, R. Wang, *et al.*, Science Bulletin **63**, 535 (2018).